PAPER

Check for updates

Structural and electronic properties of layered nanoporous organic nanocrystals†

Isaiah A. Moses [ID] [a] and Veronica Barone [ID] *[ab]

In this work, we present the optimized geometric stacking of several layered nanoporous organic nanocrystals (NONs) and the stacking effect on their electronic structure. Hexagonal layered structures, $C_{12}H_6$-h2D, $B_6N_6H_6$-h2D and C_6N_6-h2D are built from aromatic organic molecular units benzene, borazine and 1,3,5-triazine, respectively while oblique structures, $C_{10}N_2H_4$-o2D, $C_8N_4H_2$-o2D, $C_{10}P_2H_4$-o2D and $C_{10}As_2H_4$-o2D, are built from pyridine, 1,3-diazine, phosphinine and arsinine, respectively. Our density functional theory calculations show stacking energy profiles of NONs that are similar to graphene in both the stand-alone and bulk $C_{12}H_6$-h2D and $B_6N_6H_6$-h2D structures while the rest of the studied layered materials deviate from the perfect **AB** stacking. The number of layers as well as the stacking configuration significantly influence the electronic properties of these materials. Indirect to direct band gap crossovers from the bulk to monolayers are observed in all of the NONs except in C_6N_6-h2D which exhibits a direct band gap in both the monolayer, isolated few-layers, and bulk. Furthermore, it is observed that the electronic nature of $C_{10}As_2H_4$-o2D changes from a semiconducting character in the isolated monolayer to a metallic character in the bulk. The porous nature and the stability of these layered NONs combined with the electronic properties observed in this work point at them as valuable materials for potential applications in nanoelectronics and gas separation membranes, as well as deep ultraviolet optoelectronics and laser devices.

1. Introduction

Two-dimensional (2D) materials present unique features due to their reduced dimensionality which results in unusual structural, chemical, and electronic properties that are rarely found in bulk materials. These characteristics have made 2D materials a very important class of materials for technological applications such as in nanoelectronics,[1,2] optoelectronics[3,4] and photocatalysis.[5,6] A crucial electronic feature for such applications is their semiconducting character. The application of graphene for such purposes is therefore limited, despite its excellent carrier mobility as well as unique electronic, mechanical, and thermal properties,[7] since it exhibits a zero bang gap. Efforts in band gap engineering have been directed at addressing the lack of band gap in graphene through doping[8,9] strain[10,11], graphene-substrate interaction[6,12] as well as electrically gating bilayer graphene.[13] These methods, however, have been applied with a trade-off of desirable intrinsic properties of graphene. There is therefore a great interest in finding other 2D materials with finite band gaps for applications in such areas. Some examples

of 2D materials beyond graphene include C_2N-h2D,[14] phosphorene,[15,16] and transition metal dichalcogenides.[17] The electronic and optical properties of these layered materials can be also tuned by stacking two or more layers. Band gap tuning has been observed in bilayer graphene,[13,18,19] black phosphorus,[20,21] and graphene-BN heterostructures.[22] By modifying the stacking and the number of layers, a complete transition from semiconducting to metallic has been reported in some of these materials, including transition metal dichalcogenides[23] and graphene-like BC_3.[24] It is worth mentioning that while freestanding 2D materials have been shown to be corrugated,[25,26] the layered bulk units do not exhibit out-of-plane deformations.

Another important application for which 2D materials are being sought for is as separation membranes[27] since they are compact and easy to operate compared to cryogenic distillation and absorption/adsorption separation.[28–30] Graphene is not only gapless but it is also poreless. The synthesis of nanoporous graphene,[31] a graphene-like structure made out of seamlessly connected benzene units, offers an alternative in membranes for gas separation as it shows the advantage of intrinsic and well defined porosity. Nanoporous graphene has shown a high selectivity, superior to conventional polymer membranes, for H_2 and He permeability relative to other atmospheric gases such as Ne, O_2, N_2, CO, CO_2, NH_3, Ar and CH_4.[32–34]

Our recent study reported new 2D structures beyond nanoporous graphene.[35] The reported graphene-like porous

[a]Science of Advanced Materials Program, Central Michigan University, Mount Pleasant, MI 48859, USA. E-mail: v.barone@cmich.edu

[b]Department of Physics, Central Michigan University, Mount Pleasant, MI 48859, USA
† Electronic supplementary information (ESI) available. See DOI: 10.1039/d0ra08856k

materials are 2D sheets built from organic molecules other than benzene (*i.e.* borazine, pyridine, 1,2-diazine, 1,3,5-triazine, phosphinine, and arsinine) as fundamental units. They are stable monolayers with well defined small pores of typical dimensions varying from 3.1 Å to 5.94 Å and large band gaps ranging from 2.10 eV to 6.04 eV. However, little is known about the multi-layer stacking characteristics of these 2D materials.

The present study is focused on the interlayer stacking and electronic properties of these nanoporous organic nanocrystals (NONS). Understanding the interactions between layers in these systems is important for practical applications. In particular, it is important to address if the stacking and strength of the interlayer interactions differ from that of well studied graphene and other layered materials. Therefore, in this work, we utilize density functional theory (DFT) calculations to examine the interlayer interaction as well as the stacking energy profile of these novel NONs which provides an insight on the relative stability of the different stacking schemes. We also investigate how the stacking arrangement affects the electronic properties of these NONs. This study sheds light on the potential applications of NONs as membranes for gas separation as well as potential alternatives to graphene in, for example, nano-electronics and switches in electronic devices.[36,37]

2. Computational details

DFT calculations with plane-wave basis sets are carried out using the Quantum-Espresso software.[38,39] It is well known that nonlocal van der Waals interactions (vdW) in layered materials are not accounted for by traditional DFT functionals. Moreover, standard exchange functionals used within the vdW-DF overestimate the repulsion energy at shorter distances.[40] These issues have been significantly improved by the use of the generalized gradient approximation exchange functional developed by Cooper (C09$_x$)[40] in combination with the vdW correlation functional of Lee *et al.* (vdW-DF2)[41] and results with high accuracies have been reported with this method.[42] We have
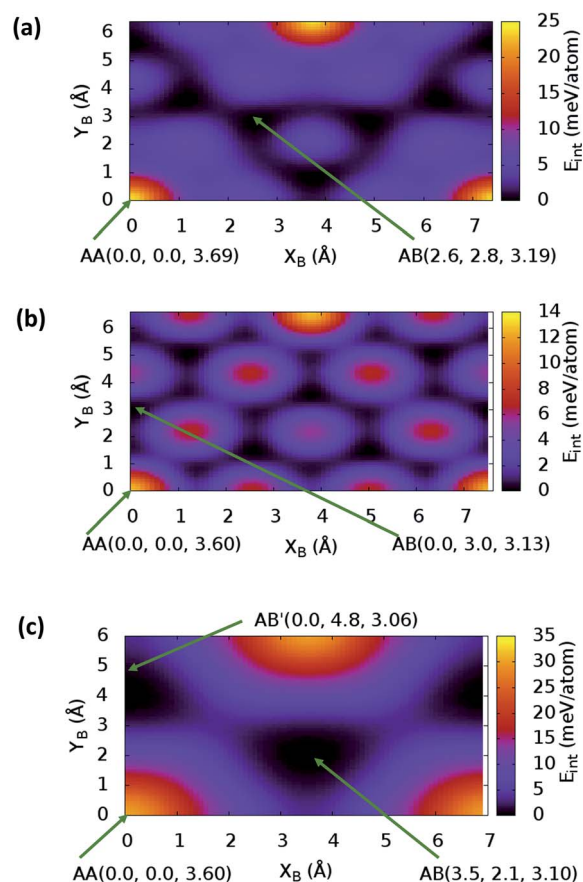

Fig. 2 Stacking energy profile for (a) bulk $C_{12}H_6$-h2D, (b) bulk $B_6N_6H_6$-h2D, and (c) bulk C_6N_6-h2D. (X_B, Y_B) is the shift in the top layer relative to the bottom layer. ($X_B = 0$, $Y_B = 0$) corresponds to the **AA** stacking. **AB'** denotes the most stable stacking in C_6N_6-h2D, which corresponds to neither **AA** nor **AB**. E_{int} values presented are relative to the most stable stacking configuration.

therefore used the vdW-DF2^{C09_x} exchange–correlation functional in our calculations in combination with norm-conserving pseudo potentials in order to replace core electrons.
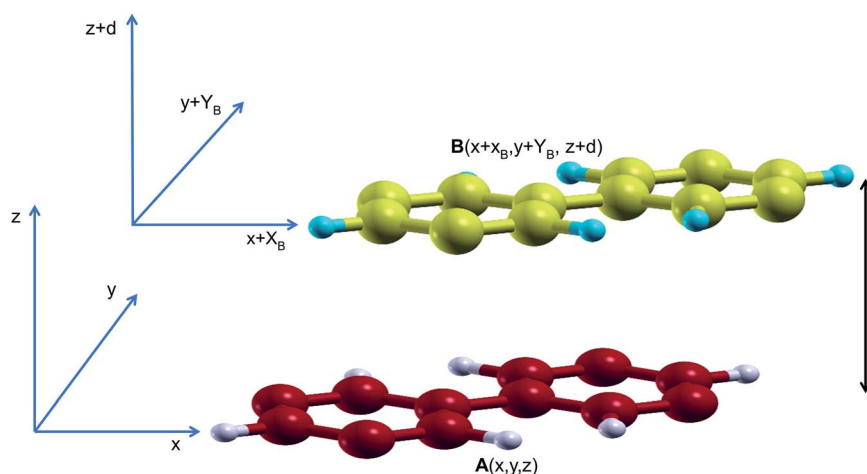

Fig. 1 Bilayer stacking scheme. Cartesian coordinates of the atoms in the bottom layer are fixed at **A**(x,y) while those for the top layer are **B**($x + X_B$, $y + Y_B$). X_B and Y_B vary from 0 to a full lattice constant a and $b \sin \gamma$, respectively so that **B**($x + a$, $y + b \sin \gamma$) corresponds to a full lattice mismatch of **B** relative to **A**.
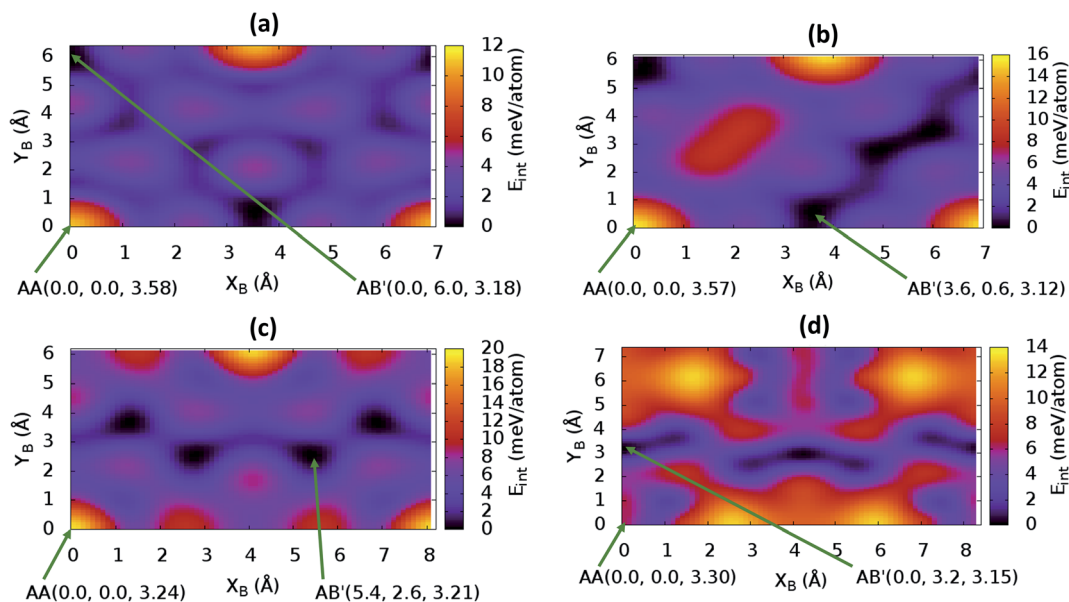
Fig. 3 Stacking energy profile in (a) bulk $C_{10}N_2H_4$-o2D, (b) bulk $C_8N_4H_2$-o2D, (c) bulk $C_{10}P_2H_4$-o2D, and (d) bulk $C_{10}As_2H_4$-o2D. (X_B, Y_B) represents the shift in the top layer relative to the bottom layer. $(X_B = 0, Y_B = 0)$ corresponds to the **AA** stacking. E_{int} values presented are relative to the most stable stacking configuration.

For each of the studied NONs, convergence tests were carried out for the kinetic energy cutoffs and the Monkhorst–Pack[43] mesh. Our assessments indicate that a kinetic energy cutoff of about 140 Ry is suitable for all the studied materials. We find that while a $14 \times 14 \times 1$ and $14 \times 14 \times 14$ Monkhorst–Pack meshes are needed for graphene and graphite, respectively, $4 \times 4 \times 1$ and $4 \times 4 \times 4$ meshes are sufficient for mono-layer and multiple layers/bulk, respectively, in the studied NONs. To model isolated two-dimensional structures we utilized a vacuum of at least 15 Å. Structural optimizations are carried out with convergence thresholds in total energy, atomic forces, and stress of 10^{-5} Ry, 10^{-3} Ry per bohr, and 0.5 kbar, respectively.
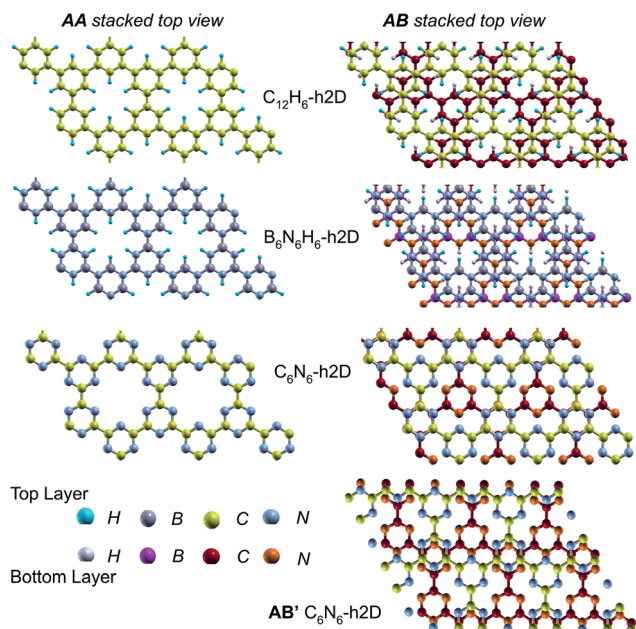

Fig. 4 Top views of **AA** and equilibrium **AB** stacked NONs. **AB′** is the equilibrium bilayer/bulk structure in C_6N_6-h2D differing from **AA** and **AB**. In the **AB** stacked structures, half of the atoms in 50% of the hexagons in the **B** layer lie directly on top of the occupied (hexagon) center of the **A** layer for both $C_{12}H_6$-h2D and $B_6N_6H_6$-h2D. In **AB** stacked C_6N_6-h2D, half of the hexagons in **B** lie directly on top of another hexagon but with C atoms on top of N atoms while the other half symmetrically occupy the pore space of layer **A**.
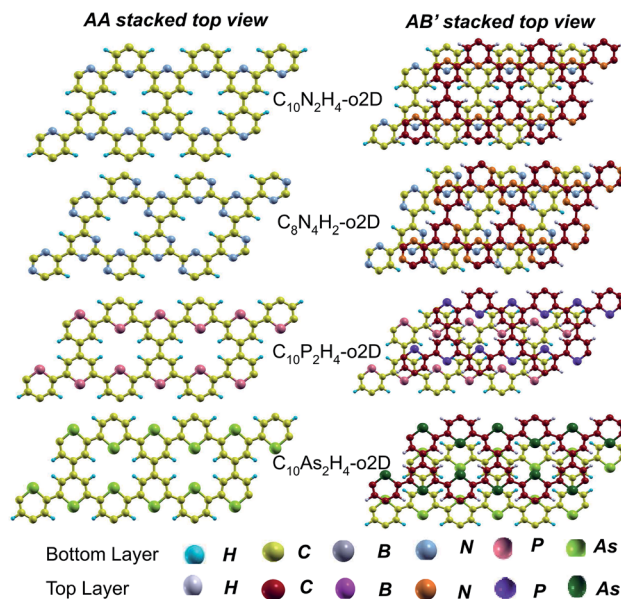

Fig. 5 Top views of **AA** and equilibrium **AB′** stacked NONs. **AB′** stacked are the equilibrium structures in the bilayer and bulk forms differing from both **AA** and **AB**.

Table 1 The interlayer separation, d (Å), and interaction energy, E_{int} (meV per atom), for stand-alone bilayers and bulk NONs. The equilibrium stacking in $C_{12}H_6$-h2D and $B_6N_6H_6$-h2D is **AB** while the stacking of the remaining systems slightly differs from **AB** and is denoted by **AB′**

	Isolated				Bulk			
	AA		**AB or AB′**		**AA**		**AB or AB′**	
Stacking	d	E_{int}	d	E_{int}	d	E_{int}	d	E_{int}
$C_{12}H_6$-h2D	3.68	10.0	3.24	13.0	3.63	22.7	3.19	37.0
$B_6N_6H_6$-h2D	3.59	10.0	3.20	15.4	3.60	22.9	3.13	36.1
C_6N_6-h2D	3.70	6.2	3.59	17.5	3.60	14.9	3.06	49.1
$C_{10}N_2H_4$-o2D	3.63	11.0	3.23	15.5	3.58	25.1	3.18	36.3
$C_8N_4H_2$-o2D	3.61	10.8	3.19	17.5	3.57	23.8	3.12	39.5
$C_{10}P_2H_4$-o2D	3.73	14.8	3.26	23.0	3.24	35.20	3.21	52.7
$C_{10}As_2H_4$-o2D	3.80	15.0	3.28	25.2	3.30	55.3	3.15	59.7
C_2N-h2D[44]			3.183	23.9			3.162	51.6

In order to study the stacking energy profile of these systems, we first define the interlayer interaction energy per atom, E_{int}, as shown in eqn (1).

$$E_{int} = \frac{\sum_i E_i - E_{cell}}{N_{cell}} \qquad (1)$$

where E_i and E_{cell} are the energies of mono-layer and the multiple-layer unit cell, respectively, i is the number of layers contained in each unit cell and N_{cell} is the total number of atoms in the unit cell. Using this definition, positive values of E_{int} imply a thermodynamically stable stacking while structures with a negative value of E_{int} are unstable. To obtain the stacking energy profile, the two layers are moved relative to each other in the xy plane as depicted in Fig. 1. The bottom and top layers are denoted as **A** and **B**, respectively. The atomic coordinates of the atoms in **A** are denoted as $A(x,y)$ while those in **B** are $B(x + X_B, y + Y_B)$. When **B** is directly above **A**, *i.e.* $X_B = 0 = Y_B$, the stacking is said to be **AA**.

In order to obtain the stacking energy profile, the atoms in **A** are kept fixed at $A(x,y)$ while those in **B** move incrementally at
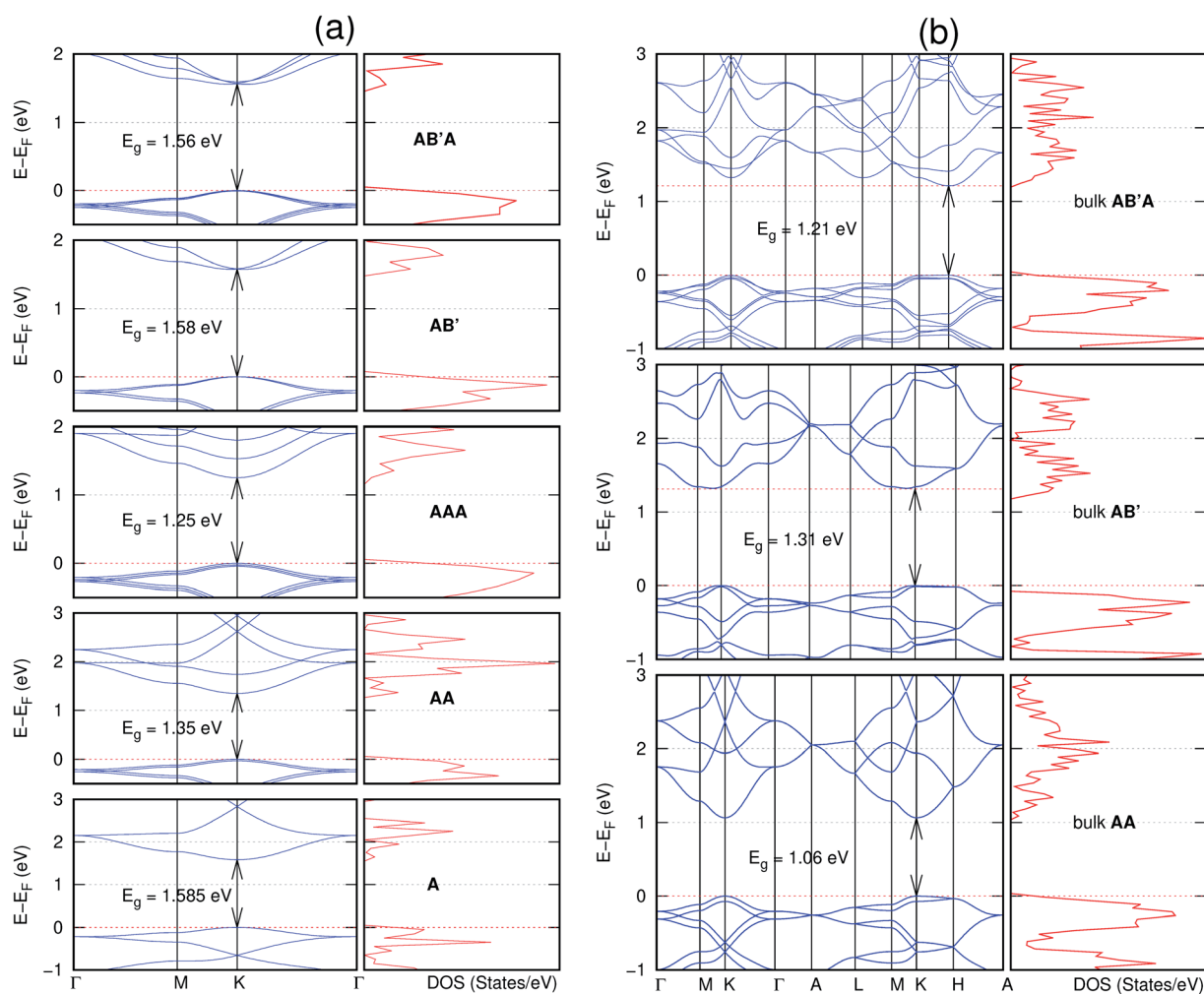

Fig. 6 Effect of stacking on the electronic structure of C_6N_6-h2D for (a) isolated one, two, and three layers with the specified stackings and (b) the bulk system with the specified stackings. The fundamental band gap is marked with an arrow that indicates their direct nature. The stacking **AB′** indicates that the most stable stacking corresponds to neither **AA** nor **AB**. The Fermi level is set at the top of the valence band.

Paper

steps of $X_B = 0.2$ Å and/or $Y_B = 0.2$ Å. In each step, the cartesian coordinates along the c lattice direction are relaxed thus providing an optimized interlayer distance d. The value of the interlayer energy is then computed for each stacking all through a full cell vector mismatch, $B(x + a, y + b \sin \gamma)$ (where a and b are the lattice parameters and γ is the angle between them), relative to $A(x, y)$.

3. Results and discussion

3.1. Stacking schemes

The stacking analysis was first carried out for graphite to establish the appropriateness of the proposed methodology. Assessment results are reported in ESI.† By exploiting the symmetry of the hexagonal NONs structures – $C_{12}H_6$-h2D, $B_6N_6H_6$-h2D and C_6N_6-h2D – built respectively from benzene, borazine and 1,3,5-triazine, it is sufficient to perform calculations for stackings from AA to a half cell vector mismatch, $B(x + a/2, y + b \sin \gamma)$ ($a = b$, $\gamma = 60°$), and use the symmetry to obtain the energies for the second half (from $B(x + a/2, y + b \sin \gamma)$ to $B(x$

$+ a, y + b \sin \gamma)$). The energy profile for the bulk structures of hexagonal symmetry are shown in Fig. 2. The energy profiles for the bulk oblique structures; $C_{10}N_2H_4$-o2D, $C_8N_4H_2$-o2D, $C_{10}P_2H_4$-o2D and $C_{10}As_2H_4$-o2D built respectively from pyridine, 1,3-diazine, phosphinine, and arsinine are shown in Fig. 3. The stacking energies presented in the figures are relative values with respect to that of the equilibrium stacking.

In addition to bulk structures, similar calculations have been carried out in bilayer systems in order to determine differences in stacking arising from bulk to few-layer structures. These energy profiles are presented in ESI (Fig. S3 and S4).† Our calculations indicate that the AA stacking is the least stable configuration for both the isolated bilayers (Fig. S3 and S4†) and the bulk structures in all systems (Fig. 2 and 3) except in bulk $C_{10}As_2H_4$-o2D (Fig. 3(d)), where AA, although not the most stable stacking, is also not the least stable arrangement. We also observe that structures where the B layer with atomic positions around the coordinates $B(x + a, y + 0.0)$ and $B(x + 0.5a, y + b \sin \gamma)$ closely follow those with B at $B(x + 0.0, y + 0.0)$ in their relatively low thermodynamic stability (Fig. 2 and 3). The most
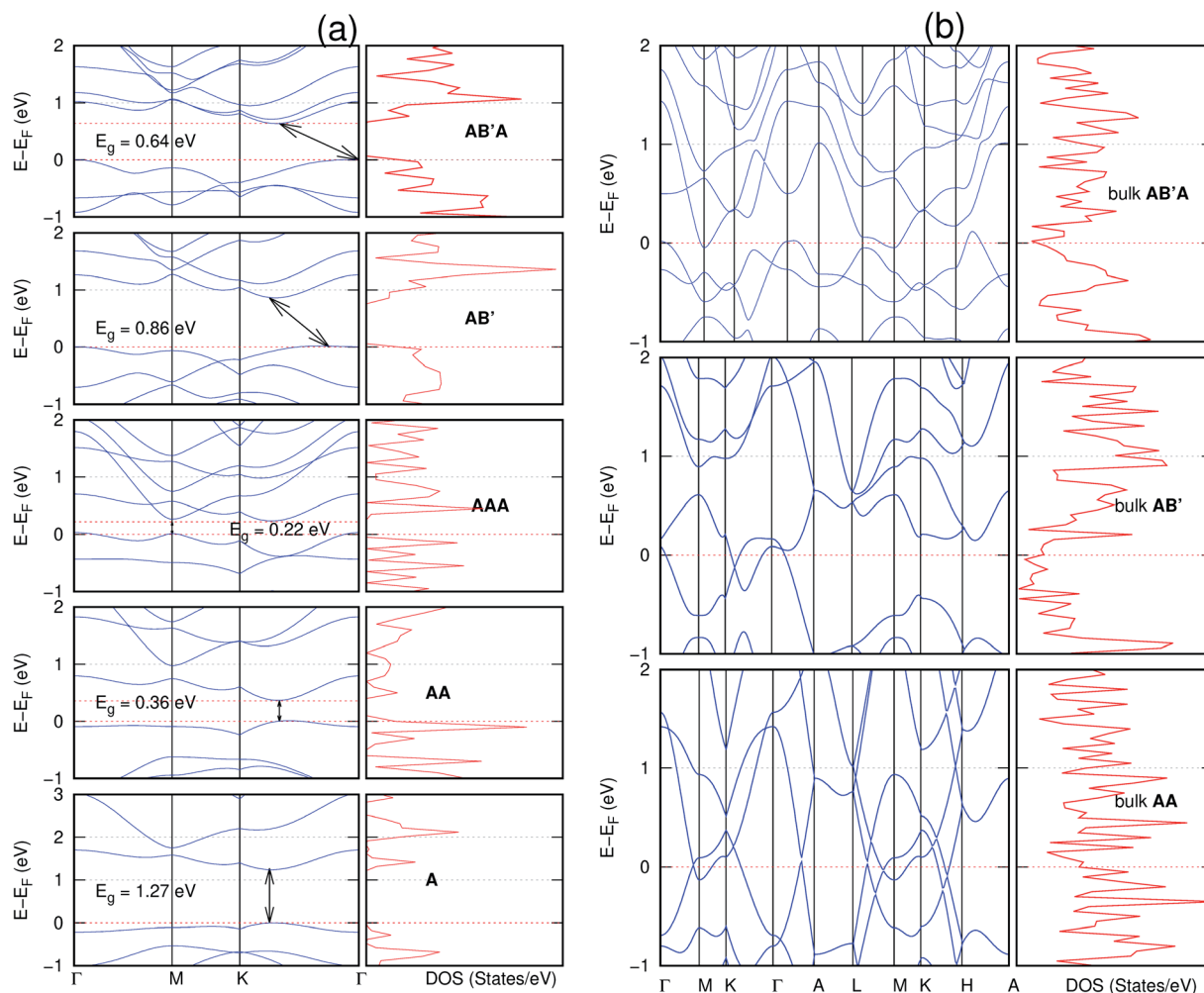

Fig. 7 Effect of stacking on the electronic structure of $C_{10}As_2H_4$-o2D for (a) isolated one, two, and three layers with the specified stackings and (b) the bulk system with the specified stackings. The fundamental band gap is marked with an arrow that indicates their direct or indirect nature. The stacking AB′ indicates that the most stable stacking corresponds to neither AA nor AB. In semiconducting systems, the Fermi level is set at the top of the valence band.

stable stackings are obtained with **B** at around $\mathbf{B}(x + 2.6, y + 2.8)$, $\mathbf{B}(x + 0.0, y + 3.0)$, and $\mathbf{B}(x + 0.0, y + 4.8)$ in the hexagonal structures $C_{12}H_6$-h2D (Fig. 2(a)), $B_6N_6H_6$-h2D (Fig. 2(b)), and C_6N_6-h2D (Fig. 2(c)), respectively, in both isolated bilayers and bulk. For the oblique structures, the **B** layer at coordinates $\mathbf{B}(x + 0.0, y + 6.0)$, $\mathbf{B}(x + 3.6, y + 0.6)$, $\mathbf{B}(x + 5.4, y + 2.6)$, and $\mathbf{B}(x + 0.0, y + 3.2)$ produce the bulk and stand-alone bilayer structures with the highest interlayer interaction energies in $C_{10}N_2H_4$-o2D (Fig. 3(a)), $C_8N_4H_2$-o2D (Fig. 3(b)), $C_{10}P_2H_4$-o2D (Fig. 3(c)), and $C_{10}As_2H_4$-o2D (Fig. 3(d)), respectively.

In the equilibrium stacking scheme of $C_{12}H_6$-h2D (Fig. 4), half of the carbon atoms in 50% of the carbon hexagons in the **B** layer are directly on top of the occupied (hexagon) center of the layer **A**. Also, carbon trigonal planes in the **B** layer symmetrically lie above the pore in **A**. In $B_6N_6H_6$-h2D **AB** stacked structures (Fig. 4), half of the atoms, consisting of boron and nitrogen, in 50% of the hexagons in **B** are directly on top of the occupied hexagon center of the layer **A** with boron on top of boron. The equilibrium stacking in $C_{12}H_6$-h2D and $B_6N_6H_6$-h2D can therefore be thought of as an **AB** type, also referred to as Bernal

stacking (Fig. 4). Other NONs with equilibrium stackings differing from **AB** are denoted as **AB′** stacked structures. The only hexagonal structure with equilibrium bulk stacking different than the Bernal stacking, C_6N_6-h2D, has an interaction energy only 0.6 meV per atom smaller than the Bernal stacking. The top views of **AA** stacked and equilibrium bilayer/bulk structures are presented in Fig. 4 for the hexagonal NONs and Fig. 5 for the obliques.

The optimum interlayer distances and the corresponding interlayer energies extracted from the energy profiles are presented in Table 1. These results show that isolated bilayers have higher values of interlayer separations and smaller interaction energies than the bulk counterparts. This trend is in agreement with previous observations in layered materials.[44] The interlayer distance of van der Waals heterostructures has been observed to also depend on the composition.[45,46] For equilibrium stackings, the values for the isolated bilayer interlayer separation ranges from 3.19 Å for $C_8N_4H_2$-o2D to about 3.59 Å for C_6N_6-h2D, while the bulk interlayer separation ranges from 3.06 Å for C_6N_6-h2D to 3.21 Å for $C_{10}P_2H_4$-o2D (Table 1). The interaction energy, on
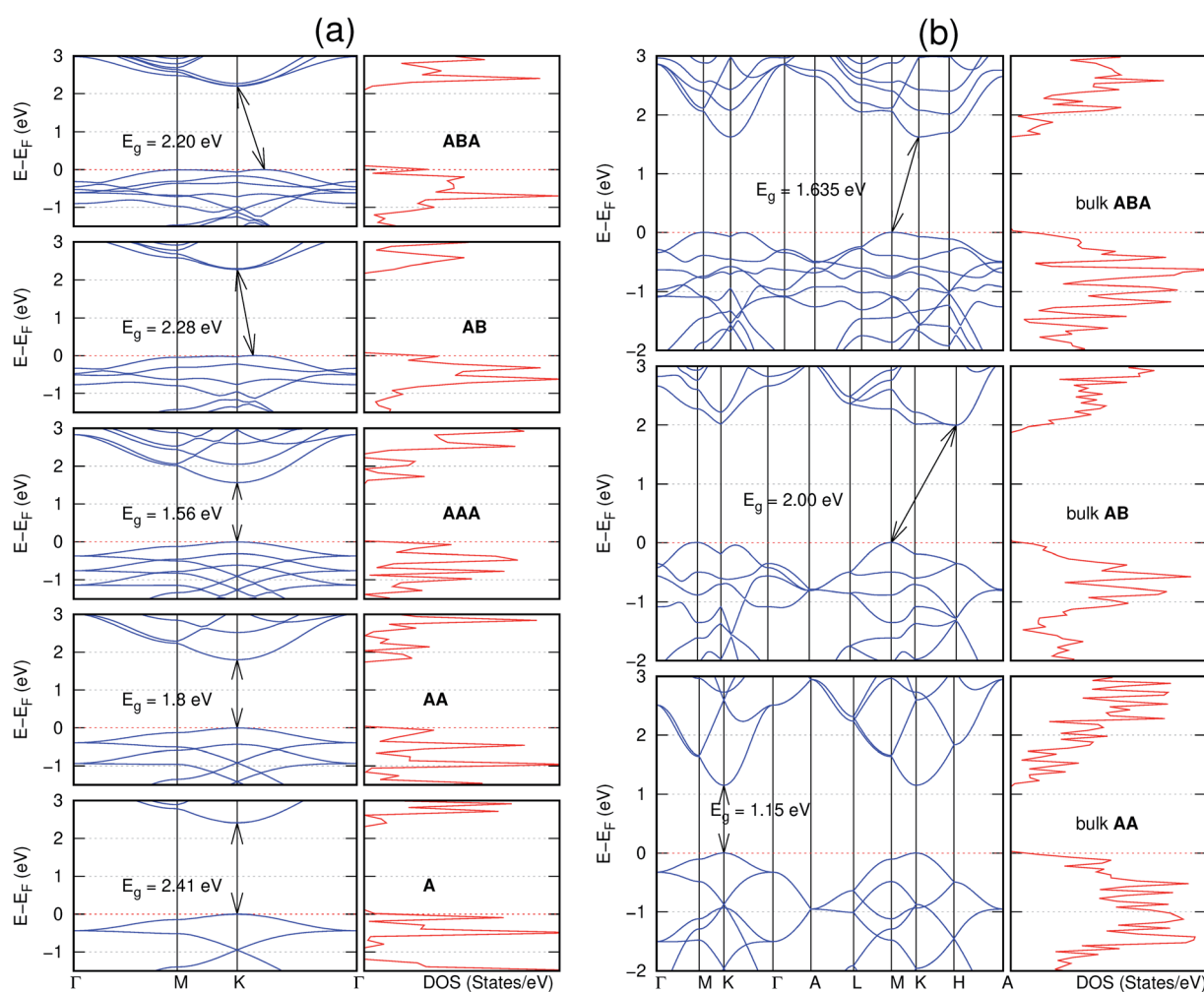

Fig. 8 Effect of stacking on the electronic structure of $C_{12}H_6$-h2D for (a) isolated one, two, and three layers with the specified stackings and (b) the bulk system with the specified stackings. The fundamental band gap is marked with an arrow that indicates their direct or indirect nature. The Fermi level is set at the top of the valence band.

the other hand, ranges from 13.0 meV per atom ($C_{12}H_6$-h2D) to 25.2 meV per atom ($C_{10}As_2H_4$-o2D) and from 36.1 meV per atom ($B_6N_6H_6$-o2D) to 59.7 meV per atom ($C_{10}As_2H_4$-o2D) for the isolated bilayer and bulk, respectively. The highest values of interaction energy is obtained for $C_{10}As_2H_4$-o2D (59.7 meV per atom), followed by $C_{10}P_2H_4$-o2D (52.7 meV per atom) (Table 1).

While the order of d cannot be readily correlated with the size of heteroatoms in all the bulk NONs, the isolated bilayers show a trend between size of heteroatom and spacing (Table 1). In particular, the similarities in the compositions of $C_{10}N_2H_4$-o2D, $C_{10}P_2H_4$-o2D and $C_{10}As_2H_4$-o2D make their comparison in terms of the sizes of the group VA atoms (N < P < As) interesting. It is observed that d for the isolated bilayers follow the same order, $C_{10}N_2H_4$-o2D < $C_{10}P_2H_4$-o2D < $C_{10}As_2H_4$-o2D, as the size of the corresponding constituent group VA atoms, the trend is more pronounced in the metastable **AA** stacked configurations (Table 1). Also, the observed trend in the interlayer interaction energies of the NONs built from the mono-substituted hetero-benzenes pyridine, phosphinine, and arsinine, can be explained on the basis of their atomic number. It is well known that

dispersion interactions originate in electron density fluctuations which give rise to instantaneous multipole moments.[47] Therefore, moving down the group VA from N to As, the increasing spatial extent of the N, P, and As lone pairs along the series[48] enhances the van der Waals interaction. It is therefore not surprising to observe an increase in the interlayer interaction energies following the order $C_{10}N_2H_4$-o2D < $C_{10}P_2H_4$-o2D < $C_{10}As_2H_4$-o2D (Table 1). Interestingly, $C_{10}As_2H_4$-o2D has a higher interaction energy than graphite while E_{int} in $C_{10}P_2H_4$-o2D is only about 3 meV per atom smaller than the corresponding value for graphite (Table S1†).

3.2. Stacking and electronic properties

In view of the known effect of stacking on the electronic properties of 2D materials[24] we studied the effect of stacking on the electronic properties of NONs. The study is carried out for monolayers (**A**), isolated bilayers and bulk stacked **AA** and the most stable stackings obtained from Section 3.1, either **AB** or **AB′**. For the bulk (isolated three layers) with the stackings **ABA**
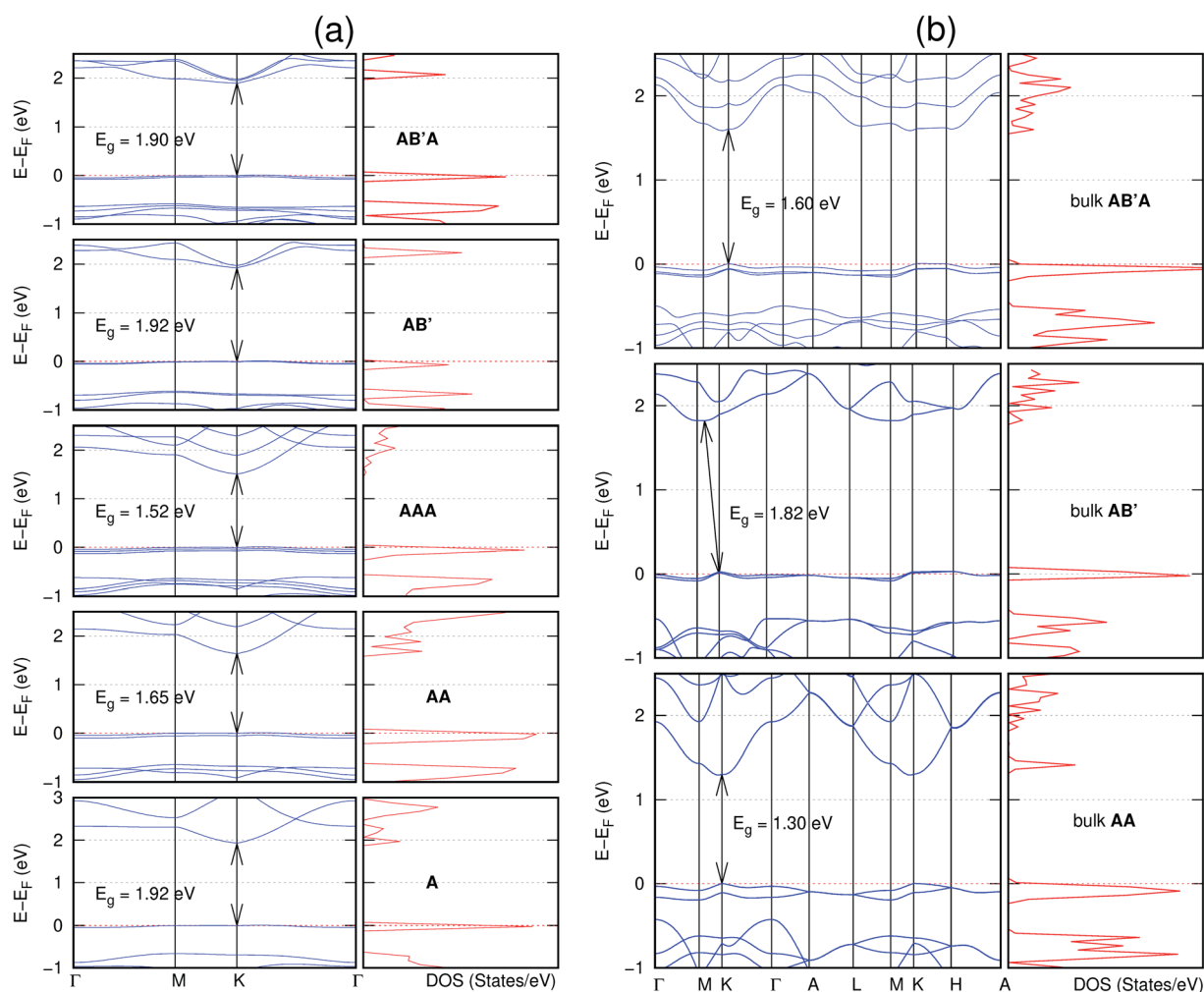

Fig. 9 Effect of stacking on the electronic structure of $C_8N_4H_2$-o2D for (a) isolated one, two, and three layers with the specified stackings and (b) the bulk system with the specified stackings. The fundamental band gap is marked with an arrow that indicates their direct or indirect nature. The stacking AB′ indicates that the most stable stacking corresponds to neither AA nor AB. The Fermi level is set at the top of the valence band.

or **AB′A**, these are built from the most stable bulk (isolated bilayers) with the stackings **AB** and **AB′** respectively. The band structures of the isolated and bulk NONs were obtained along high symmetry k-points paths of the Brillouin zone.[49] The density of states (DOS) for each of the studied materials was also calculated.

The number of layers and the stacking order are observed to have a significant effect on the electronic properties of the studied NONs (Fig. 6–12) due to the band splitting originating from the orbital interaction between the layers.[44] Due to the exchange-correlation functional used in the present work, the values of the band gaps (E_g) are underestimated compared to our previous results obtained using the HSE hybrid functional.[35] However, as shown in the latter (Tables 1 and 2 in ESI†) the overall trends in E_g should be well represented by the chosen functional.

All monolayers present a direct band gap (Fig. 6–12 with label **A**). These values monotonically decrease as the number of layers increase. Additionally, the magnitude of the band gap

also depends on the geometric stacking, with the **AA** stacked structures presenting a larger decrease in E_g (ΔE_g) than those with a mismatch between at least two consecutive layers. Examining the ΔE_g with increasing layer numbers (from single to three layers) of the different materials, we observe that C_6N_6-h2D (Fig. 6) has the smallest response to the number of layers. While it's monolayer has E_g of 1.585 eV, the **AA** stacked bilayer and trilayer has values of 1.35 eV and 1.25 eV respectively. The ΔE_g between the monolayer and trilayer is therefore 0.33 eV. The ΔE_g for the $C_8N_4H_2$-o2D structure (Fig. 9) is 0.40 eV. The values of the ΔE_g for the rest of the NONs are significantly higher. $C_{10}P_2H_4$-o2D (Fig. 10), for instance, presents the largest ΔE_g value of 1.10 eV.

The order of stacking of the layers also determine the values and, for some of the NONs, the nature of the E_g in the bulk structures (Fig. 6–12). As in the case for the isolated layers, **AA** stacked bulk materials possess lower E_g than those built with a mismatch between the layers. For NONs that are semiconducting in their bulk forms as well as in the isolated
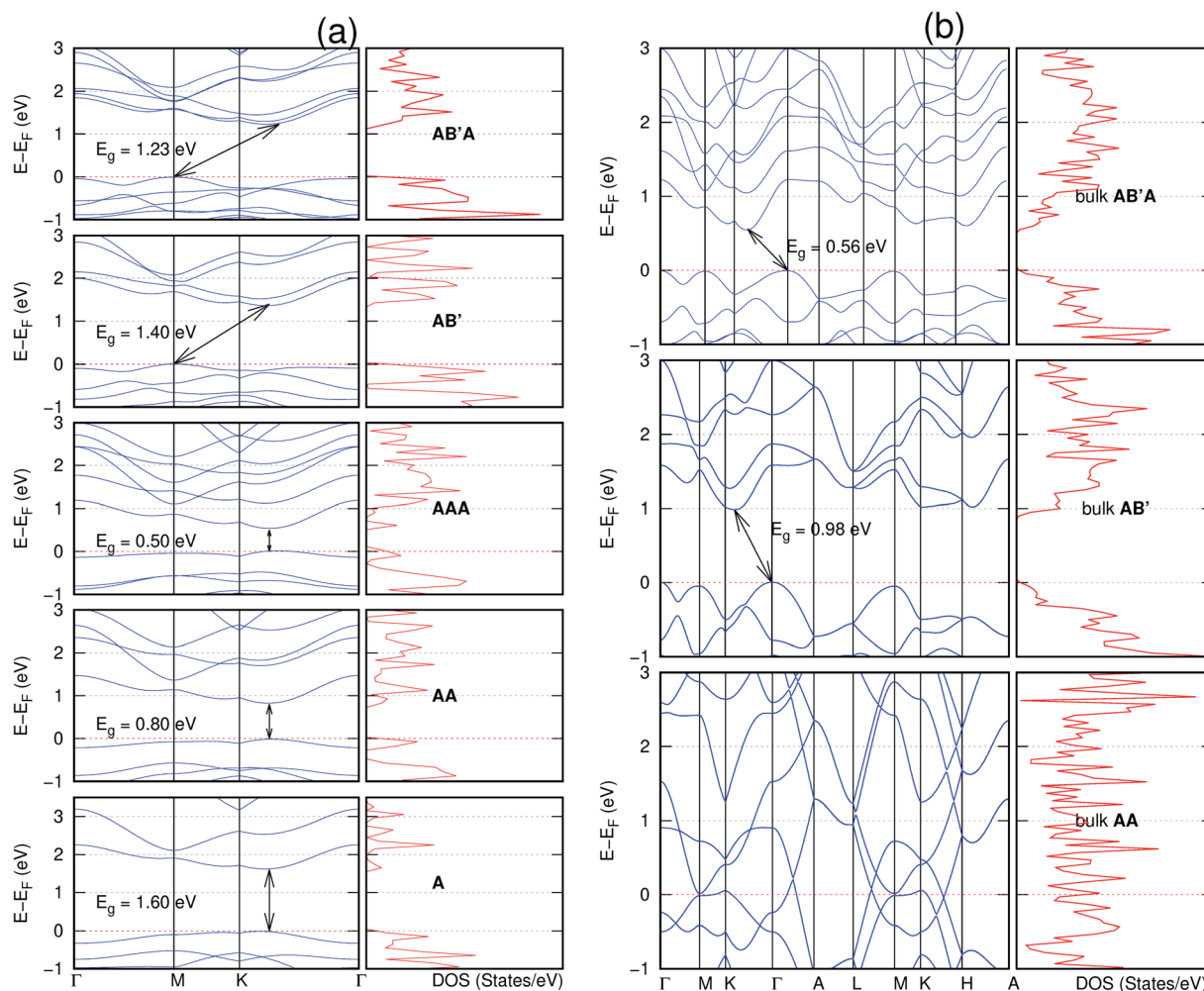

Fig. 10 Effect of stacking on the electronic structure of $C_{10}P_2H_4$-o2D for (a) isolated one, two, and three layers with the specified stackings and (b) the bulk system with the specified stackings. The fundamental band gap is marked with an arrow that indicates their direct or indirect nature. The stacking **AB′** indicates that the most stable stacking corresponds to neither **AA** nor **AB**. In semiconducting systems, the Fermi level is set at the top of the valence band.

multiple-layers, the most stable stacking configurations – **AB** or **AB**′ – presents the widest E_g among the different stacking orders considered. An indirect to direct E_g crossover from the bulk to monolayer is observed in all the NONs except in C_6N_6-h2D (Fig. 6) and $C_{10}As_2H_4$-o2D (Fig. 7). The same phenomenon has been observed experimentally in other layered materials including h-BN[50] and MoS_2.[51] In particular, $C_{12}H_6$-h2D (Fig. 8) and $B_6N_6H_6$-h2D (Fig. 11) exhibit the same trends in all stacking configurations studied. Their monolayers and **AA** stacked multiple-layers and bulk structures show direct E_g while **AB** and **ABA** stacked structures exhibit an indirect E_g.

Interestingly, the electronic properties of the structure obtained from pyridine ($C_{10}N_2H_4$-o2D) (Fig. 12) shows a different E_g nature than those of benzene ($C_{12}H_6$-h2D) (Fig. 8) and borazine ($B_6N_6H_6$-h2D) (Fig. 11). Only its monolayer presents a direct band gap while all others, both in the isolated and bulk forms, present indirect E_g. With one more C atom substituted by N (1,3-diazine), only the **AB**′ stacked bulk of the corresponding structure ($C_8N_4H_2$-o2D) (Fig. 9) exhibits an indirect E_g. Further substitution of one C atom by N (rendering 1,3,5-triazine) results in C_6N_6-hD with direct E_g for the monolayer,

few layers and bulk, irrespective of the stacking arrangement (Fig. 6). A similar structure with the same chemical constituents, C_2N-h2D, has also been reported to exhibit a direct E_g both in the monolayer and bulk forms.[44]

It is interesting to note that, while the features exhibited by $C_{10}P_2H_4$-o2D (Fig. 10) and $C_{10}As_2H_4$-o2D (Fig. 7) are similar to those of $C_{12}H_6$-h2D (Fig. 8) and $B_6N_6H_6$-h2D (Fig. 11) in terms of layer order effect on the relative position of the valence band maximum (VBM) and the conduction band minimum (CBM) (direct or indirect), $C_{10}P_2H_4$-o2D presents a metallic character in the metastable **AA** bulk and $C_{10}As_2H_4$-o2D exhibits a metallic character in the bulk irrespective of the stacking arrangement.

The observed significant tuning of the electronic properties with layer number and stacking order in these materials is a result of the splitting of the bands induced mainly by the interaction of atomic orbitals between the layers. It can be inferred that the chemical composition of the materials as well as the spatial matching of the bands of different layers arising from the stacking schemes have a significant influence on the nature of the band structure.
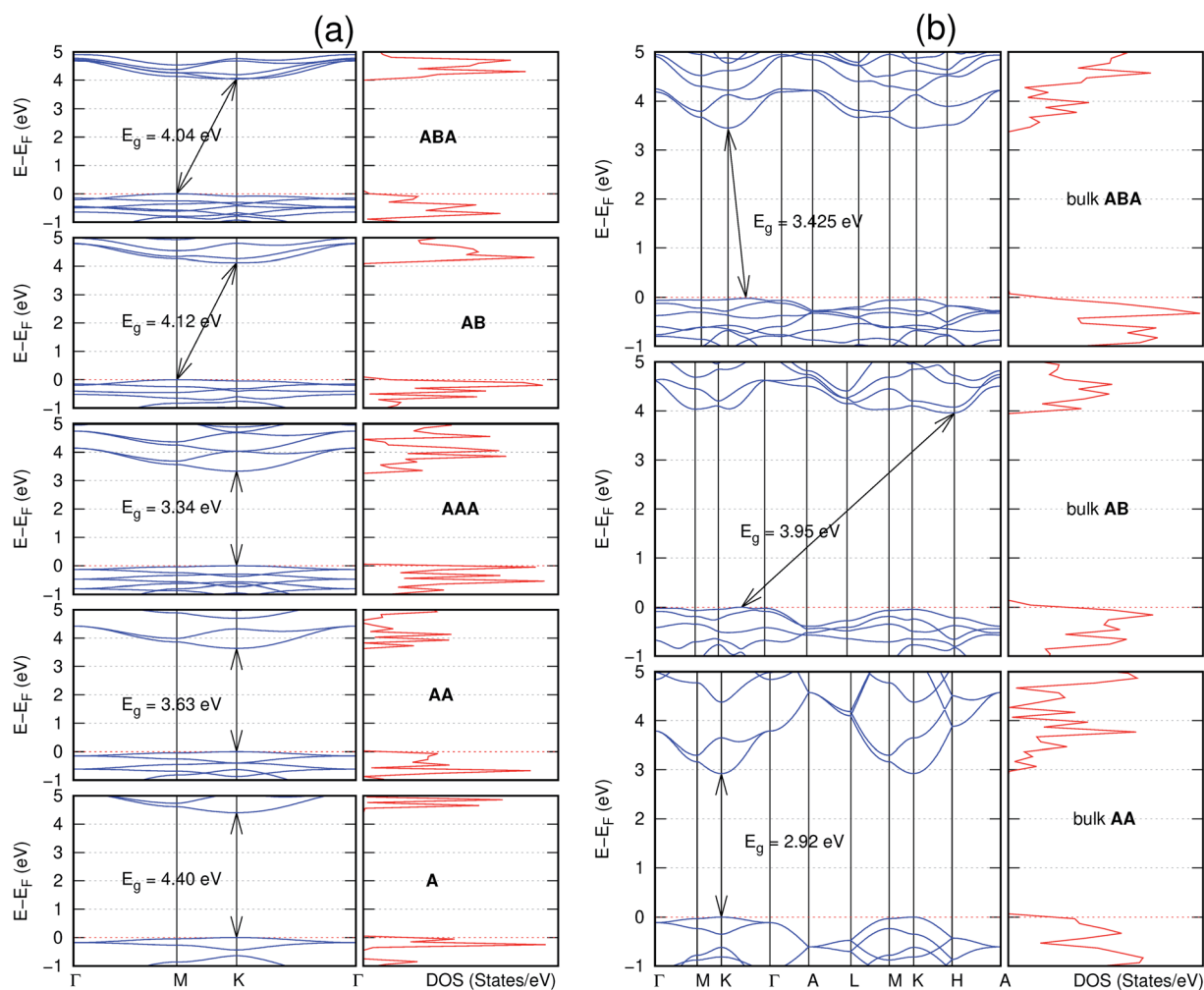

Fig. 11 Effect of stacking on the electronic structure of $B_6N_6H_6$-h2D for (a) isolated one, two, and three layers with the specified stackings and (b) the bulk system with the specified stackings. The fundamental band gap is marked with an arrow that indicates their direct or indirect nature. The Fermi level is set at the top of the valence band.
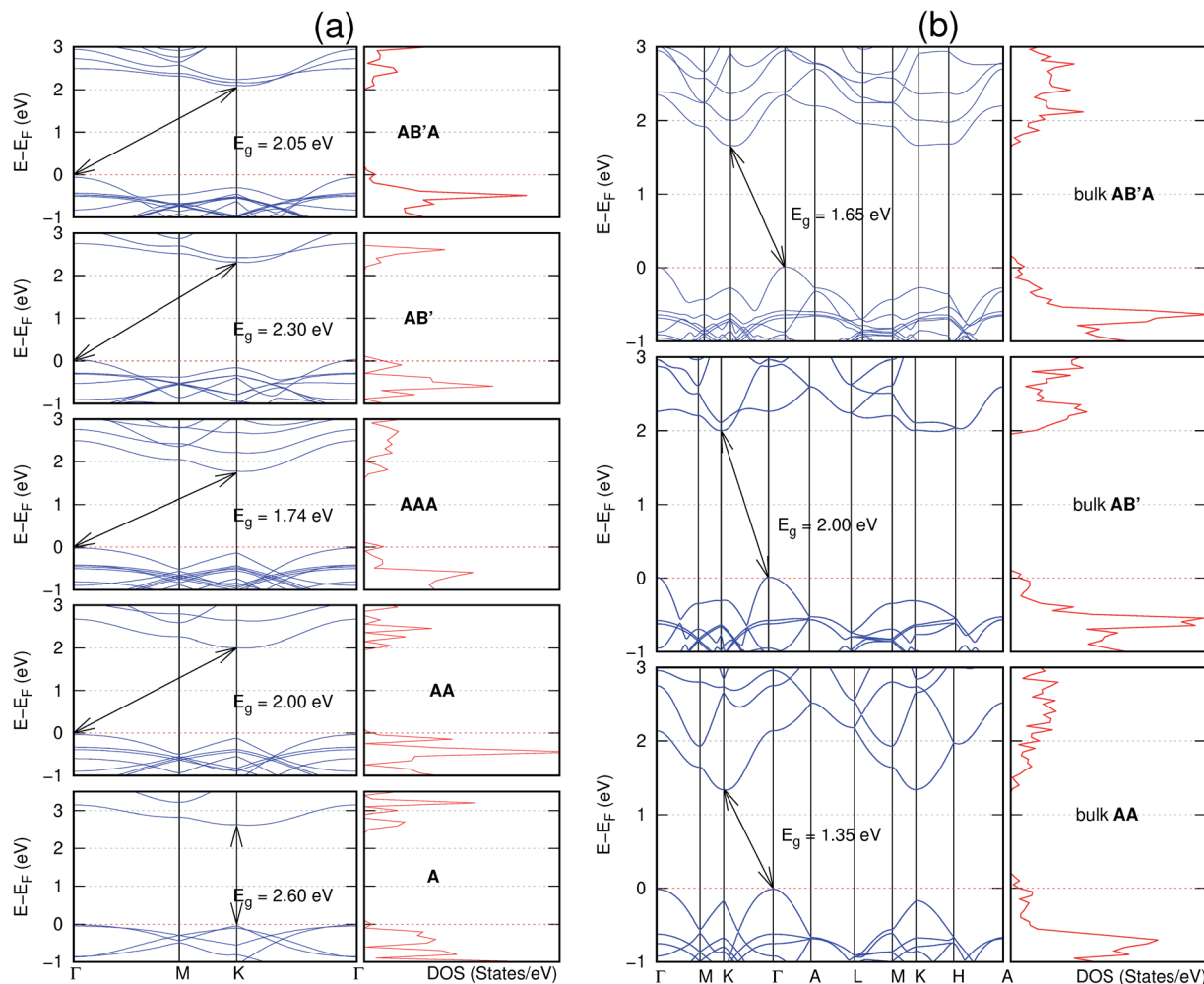
Fig. 12 Effect of stacking on the electronic structure of $C_{10}N_2H_4$-o2D for (a) isolated one, two, and three layers with the specified stackings and (b) the bulk system with the specified stackings. The fundamental band gap is marked with an arrow that indicates their direct or indirect nature. The stacking **AB'** indicates that the most stable stacking corresponds to neither **AA** nor **AB**. The Fermi level is set at the top of the valence band.

Comparing $B_6N_6H_6$-h2D and the well-studied h-BN, we have previously reported a small lattice mismatch of 1.2% in their monolayer.[35] Also observed previously is the E_g in the ultraviolet region of 6.07 eV and 6.04 eV for $B_6N_6H_6$-h2D and h-BN, respectively. A similar direct-to-indirect E_g crossover from mono layer to bulk in h-BN[50] is also observed in $B_6N_6H_6$-h2D (Fig. 11). Therefore, just as h-BN, $B_6N_6H_6$-h2D could prove promising for deep ultraviolet optoelectronic and laser devices applications.[50,52]

Some of these NONs present flat bands and the corresponding peaks in density of states at the Fermi level. This is especially pronounced in the NONs containing H and high concentration of N, $B_6N_6H_6$-h2D (Fig. 11) and $C_8N_4H_2$-o2D (Fig. 9). We were therefore interested in investigating what orbitals are responsible for the localized states. Projected density of states for the monolayer and equilibrium bulk $B_6N_6H_6$-h2D and $C_8N_4H_2$-o2D were therefore obtained. The monolayer (Fig. S5(a)†) and bulk (Fig. S5(b)†) $B_6N_6H_6$-h2D as well as the monolayer (Fig. S5(c)†) and bulk (Fig. S5(d)†) $C_8N_4H_2$-o2D shows that p bands from the N atom are

responsible for the peaks in the density of states around the Fermi level.

4. Conclusions

We have studied the stacking energy profiles and the effect of stacking on the electronic properties of nanoporous organic nanocrystals (NONs) built from organic molecular units. Comprehensive stacking energy profiles show that the **AA** stacked structures are the least stable configurations in all of the studied NONs except in the case of $C_{10}As_2H_4$-o2D. The equilibrium stacking obtained in both $C_{12}H_6$-h2D and $B_6N_6H_6$-h2D is observed to be of the Bernal type while the preferred stacking for the rest of the hexagonal (C_6N_6-h2D) and oblique structures ($C_{10}N_2H_4$-o2D, $C_8N_4H_2$-o2D, $C_{10}P_2H_4$-o2D and $C_{10}As_2H_4$-o2D) is observed to slightly deviate from a perfect **AB** stacking. Our DFT calculations show that the isolated bilayers present interaction energies varying from 13.0 meV per atom to 25.2 meV per atom while the values for the bulk counterparts vary from 36.1 meV per atom to 59.7 meV per atom. Calculations

indicate a significant effect of the stacking configuration and the number of layers on the electronic properties of the studied materials. We observe that the band gap monotonically decreases as the number of layers increases. Indirect to direct band gap crossovers from bulk to monolayers are also observed in all of the NONs except in C_6N_6-h2D which exhibits a direct band gap in both monolayer, isolated few-layers, and bulk. Additionally, it is observed that the electronic nature of $C_{10}As_2H_4$-o2D changes from a semiconducting character in the isolated monolayer to a metallic character in the bulk. The porous nature and the stability of these layered NONs combined with the electronic properties observed in this work point at them as valuable materials for potential applications in nano-electronics and gas separation membranes, as well as deep ultraviolet optoelectronics and laser devices.

Conflicts of interest

There are no conflicts to declare.

Acknowledgements

References

1 M. Osada and T. Sasaki, Two-dimensional dielectric nanosheets: novel nanoelectronics from nanocrystal building blocks, *Adv. Mater.*, 2012, **24**(2), 210–228.

2 D. Akinwande, N. Petrone and J. Hone, Two-dimensional flexible nanoelectronics, *Nat. Commun.*, 2014, **5**(1), 1–12.

3 K. F. Mak and J. Shan, Photonics and optoelectronics of 2D semiconductor transition metal dichalcogenides, *Nat. Photonics*, 2016, **10**(4), 216.

4 Q. H. Wang, K. Kalantar-Zadeh, A. Kis, J. N. Coleman and M. S. Strano, Electronics and optoelectronics of two-dimensional transition metal dichalcogenides, *Nat. Nanotechnol.*, 2012, **7**(11), 699.

5 A. K. Singh, K. Mathew, H. L. Zhuang and R. G. Hennig, Computational screening of 2D materials for photocatalysis, *J. Phys. Chem. Lett.*, 2015, **6**(6), 1087–1098.

6 B. Luo, G. Liu and L. Wang, Recent advances in 2D materials for photocatalysis, *Nanoscale*, 2016, **8**(13), 6904–6920.

7 D. Akinwande, N. Petrone and J. Hone, Two-dimensional flexible nanoelectronics, *Nat. Commun.*, 2014, **5**, 5678.

8 C.-K. Chang, S. Kataria, C.-C. Kuo, A. Ganguly, B.-Y. Wang, J.-Y. Hwang, K.-J. Huang, W.-H. Yang, S.-B. Wang, C.-H. Chuang, *et al.*, Band gap engineering of chemical vapor deposited graphene by in situ BN doping, *ACS Nano*, 2013, **7**(2), 1333–1341.

9 Y. Shi, K. K. Kim, A. Reina, M. Hofmann, L.-J. Li and J. Kong, Work function engineering of graphene electrode via chemical doping, *ACS Nano*, 2010, **4**(5), 2689–2694.

10 G. Gui, J. Li and J. Zhong, Band structure engineering of graphene by strain: first-principles calculations, *Phys. Rev. B*, 2008, **78**(7), 075435.

11 I. Naumov and A. Bratkovsky, Gap opening in graphene by simple periodic inhomogeneous strain, *Phys. Rev. B*, 2011, **84**(24), 245444.

12 G. Giovannetti, P. A. Khomyakov, G. Brocks, P. J. Kelly and J. Van Den Brink, Substrate-induced band gap in graphene on hexagonal boron nitride: ab initio density functional calculations, *Phys. Rev. B*, 2007, **76**(7), 073103.

13 E. V. Castro, K. Novoselov, S. Morozov, N. Peres, J. L. Dos Santos, J. Nilsson, F. Guinea, A. Geim and A. C. Neto, Biased bilayer graphene: semiconductor with a gap tunable by the electric field effect, *Phys. Rev. Lett.*, 2007, **99**(21), 216802.

14 J. Mahmood, E. K. Lee, M. Jung, D. Shin, I.-Y. Jeon, S.-M. Jung, H.-J. Choi, J.-M. Seo, S.-Y. Bae, S.-D. Sohn, *et al.*, Nitrogenated holey two-dimensional structures, *Nat. Commun.*, 2015, **6**, 6486.

15 H. Liu, A. T. Neal, Z. Zhu, Z. Luo, X. Xu, D. Tomãnek and P. D. Ye, Phosphorene: an unexplored 2D semiconductor with a high hole mobility, *ACS Nano*, 2014, **8**(4), 4033–4041.

16 L. Li, Y. Yu, G. J. Ye, Q. Ge, X. Ou, H. Wu, D. Feng, X. H. Chen and Y. Zhang, Black phosphorus field-effect transistors, *Nat. Nanotechnol.*, 2014, **9**(5), 372.

17 B. Radisavljevic, A. Radenovic, J. Brivio, V. Giacometti and A. Kis, Single-layer MoS_2 transistors, *Nat. Nanotechnol.*, 2011, **6**(3), 147.

18 Y. Zhang, T.-T. Tang, C. Girit, Z. Hao, M. C. Martin, A. Zettl, M. F. Crommie, Y. R. Shen and F. Wang, Direct observation of a widely tunable bandgap in bilayer graphene, *Nature*, 2009, **459**(7248), 820.

19 F. Xia, D. B. Farmer, Y.-m. Lin and P. Avouris, Graphene field-effect transistors with high on/off current ratio and large transport band gap at room temperature, *Nano Lett.*, 2010, **10**(2), 715–718.

20 J. Kim, S. S. Baik, S. H. Ryu, Y. Sohn, S. Park, B.-G. Park, J. Denlinger, Y. Yi, H. J. Choi and K. S. Kim, Observation of tunable band gap and anisotropic dirac semimetal state in black phosphorus, *Science*, 2015, **349**(6249), 723–726.

21 D. Çakır, C. Sevik and F. M. Peeters, Significant effect of stacking on the electronic and optical properties of few-layer black phosphorus, *Phys. Rev. B*, 2015, **92**(16), 165406.

22 A. Ramasubramaniam, D. Naveh and E. Towe, Tunable band gaps in bilayer graphene–BN heterostructures, *Nano Lett.*, 2011, **11**(3), 1070–1075.

23 N. Lu, H. Guo, L. Li, J. Dai, L. Wang, W.-N. Mei, X. Wu and X. C. Zeng, MoS_2/MX_2 heterobilayers: bandgap engineering via tensile strain or external electrical field, *Nanoscale*, 2014, **6**(5), 2879–2886.

24 B. Ozdemir and V. Barone, Structural and electronic properties of crystalline graphite-like BC_3, *Comput. Mater. Sci.*, 2015, **109**, 248–252.

25 A. Fasolino, J. Los and M. I. Katsnelson, Intrinsic ripples in graphene, *Nat. Mater.*, 2007, **6**(11), 858–861.

26 J. C. Meyer, A. K. Geim, M. I. Katsnelson, K. S. Novoselov, T. J. Booth and S. Roth, The structure of suspended graphene sheets, *Nature*, 2007, **446**(7131), 60–63.

27 F. Moghadam and H. B. Park, 2D nanoporous materials: membrane platform for gas and liquid separations, *2D Mater.*, 2019, **6**(4), 042002.

28 L. M. Robeson, Polymer membranes for gas separation, *Curr. Opin. Solid State Mater. Sci.*, 1999, **4**(6), 549–552.

29 L. Wang, M. S. Boutilier, P. R. Kidambi, D. Jang, N. G. Hadjiconstantinou and R. Karnik, Fundamental transport mechanisms, fabrication and potential applications of nanoporous atomically thin membranes, *Nat. Nanotechnol.*, 2017, **12**(6), 509.

30 M. G. Buonomenna, Membrane processes for a sustainable industrial growth, *RSC Adv.*, 2013, **3**(17), 5694–5740.

31 M. Bieri, M. Treier, J. Cai, K. Ait-Mansour, P. Ruffieux, O. Gröning, P. Gröning, M. Kastler, R. Rieger, X. Feng and K. Müllen, Porous graphenes: two-dimensional polymer synthesis with atomic precision, *Chem. Commun.*, 2009, **45**, 6919–6921.

32 Y. Li, Z. Zhou, P. Shen and Z. Chen, Two-dimensional polyphenylene: experimentally available porous graphene as a hydrogen purification membrane, *Chem. Commun.*, 2010, **46**(21), 3672–3674.

33 S. Blankenburg, M. Bieri, R. Fasel, K. Müllen, C. A. Pignedoli and D. Passerone, Porous graphene as an atmospheric nanofilter, *Small*, 2010, **6**(20), 2266–2271.

34 J. Schrier, Helium separation using porous graphene membranes, *J. Phys. Chem. Lett.*, 2010, **1**(15), 2284–2287.

35 V. Barone and I. A. Moses, Structure and stability of graphene-like layers built from heterocyclic units, *Carbon*, 2019, (152), 128–133.

36 P. Solis-Fernandez, M. Bissett and H. Ago, Synthesis, structure and applications of graphene-based 2D heterostructures, *Chem. Soc. Rev.*, 2017, **46**(15), 4572–4613.

37 T. Ohta, A. Bostwick, T. Seyller, K. Horn and E. Rotenberg, Controlling the electronic structure of bilayer graphene, *Science*, 2006, **313**(5789), 951–954.

38 P. Giannozzi, S. Baroni, N. Bonini, M. Calandra, R. Car, C. Cavazzoni, D. Ceresoli, G. L. Chiarotti, M. Cococcioni, I. Dabo, *et al.*, QUANTUM ESPRESSO: a modular and open-source software project for quantum simulations of materials, *J. Phys.: Condens. Matter*, 2009, **21**(39), 395502.

39 P. Giannozzi, O. Andreussi, T. Brumme, O. Bunau, M. B. Nardelli, M. Calandra, R. Car, C. Cavazzoni, D. Ceresoli, M. Cococcioni, *et al.*, Advanced capabilities for materials modelling with Quantum ESPRESSO, *J. Phys.: Condens. Matter*, 2017, **29**(46), 465901.

40 V. R. Cooper, van der waals density functional: an appropriate exchange functional, *Phys. Rev. B*, 2010, **81**(16), 161104.

41 K. Lee, É. D. Murray, L. Kong, B. I. Lundqvist and D. C. Langreth, Higher-accuracy van der waals density functional, *Phys. Rev. B*, 2010, **82**(8), 081101.

42 I. Hamada and M. Otani, Comparative van der waals density-functional study of graphene on metal surfaces, *Phys. Rev. B*, 2010, **82**(15), 153412.

43 H. J. Monkhorst and J. D. Pack, Special points for Brillouin-zone integrations, *Phys. Rev. B*, 1976, **13**(12), 5188.

44 R. Zhang, B. Li and J. Yang, Effects of stacking order, layer number and external electric field on electronic structures of few-layer C_2N-h2D, *Nanoscale*, 2015, **7**(33), 14062–14070.

45 O. Kurakevych, T. Chauveau and V. Solozhenko, On crystal lattice parameters of graphite-like phases of the bc system, *J. Superhard Mater.*, 2010, **32**(4), 231–235.

46 J. Kouvetakis, T. Sasaki, C. Shen, R. Hagiwara, M. Lerner, K. Krishnan and N. Bartlett, Novel aspects of graphite intercalation by fluorine and fluorides and new B/C, C/N and B/C/N materials based on the graphite network, *Synth. Met.*, 1989, **34**(1–3), 1–7.

47 A. M. Reilly and A. Tkatchenko, van der waals dispersion interactions in molecular materials: beyond pairwise additivity, *Chem. Sci.*, 2015, **6**(6), 3289–3301.

48 C. Müller, L. E. Broeckx, I. de Krom and J. J. Weemers, Developments in the coordination chemistry of phosphinines, *Eur. J. Inorg. Chem.*, 2013, (2), 187–202.

49 W. Setyawan and S. Curtarolo, High-throughput electronic band structure calculations: challenges and tools, *Comput. Mater. Sci.*, 2010, **49**(2), 299–312.

50 C. Elias, P. Valvin, T. Pelini, A. Summerfield, C. Mellor, T. Cheng, L. Eaves, C. Foxon, P. Beton, S. Novikov, *et al.*, Direct band-gap crossover in epitaxial monolayer boron nitride, *Nat. Commun.*, 2019, **10**(1), 2639.

51 K. F. Mak, C. Lee, J. Hone, J. Shan and T. F. Heinz, Atomically thin MoS_2: a new direct-gap semiconductor, *Phys. Rev. Lett.*, 2010, **105**(13), 136805.

52 K. Watanabe, T. Taniguchi and H. Kanda, Direct-bandgap properties and evidence for ultraviolet lasing of hexagonal boron nitride single crystal, *Nat. Mater.*, 2004, **3**(6), 404.